Quasifree (p,pN) scattering of light neutron-rich nuclei near N=14

P. Díaz Fernández *et al.* (R3B Collaboration)

Quasi-free (p,pN) scattering of light neutron-rich nuclei around $N = 14$

P. Díaz Fernández,[1,2,3] H. Alvarez-Pol,[2,3] R. Crespo,[4,5] E. Cravo,[6] L. Atar,[7] A. Deltuva,[8] T. Aumann,[7,9]
V. Avdeichikov,[10] S. Beceiro-Novo,[11] D. Bemmerer,[12] J. Benlliure,[2,3] C. A. Bertulani,[13] J. M. Boillos,[2,3]
K. Boretzky,[9] M. J. G. Borge,[14] M. Caamaño,[2,3] P. Cabanelas,[2,3] C. Caesar,[7,9] E. Casarejos,[15] W. Catford,[16]
J. Cederkäll,[10] M. Chartier,[17] L. V. Chulkov,[18] D. Cortina-Gil,[2,3] U. Datta Pramanik,[19] I. Dillmann,[20,9]
Z. Elekes,[12] J. Enders,[7] O. Ershova,[21] A. Estradé,[9,22] F. Farinon,[9] B. Fernández-Domínguez,[2,3] L. M. Fraile,[23]
M. Freer,[24] D. Galaviz,[25,26] H. Geissel,[9] R. Gernhäuser,[27] P. Golubev,[10] K. Göbel,[21] J. Hagdahl,[1]
T. Heftrich,[21] M. Heil,[9] M. Heine,[7] A. Heinz,[1] A. Henriques,[25] M. Holl,[7] A. Hufnagel,[7] A. Ignatov,[7]
H. T. Johansson,[1] B. Jonson,[1] D. Jurčiukonis,[8] N. Kalantar-Nayestanaki,[28] R. Kanungo,[22] A. Kelic-Heil,[9]
A. Knyazev,[10] T. Kröll,[7] N. Kurz,[9] M. Labiche,[29] C. Langer,[21] T. Le Bleis,[27] R. Lemmon,[29] S. Lindberg,[1]
J. Machado,[30] J. Marganiec,[7,31,9] A. M. Moro,[32] A. Movsesyan,[7] E. Nacher,[14] A. Najafi,[28] E. Nikolskii,[18]
T. Nilsson,[1] C. Nociforo,[9] V. Panin,[7] S. Paschalis,[7,33] A. Perea,[14] M. Petri,[7,33] B. Pietras,[2,3] S. Pietri,[9]
R. Plag,[21] R. Reifarth,[21] G. Ribeiro,[14] C. Rigollet,[28] D. Rossi,[9] M. Röder,[34,12] D. Savran,[31,35]
H. Scheit,[7] H. Simon,[9] O. Sorlin,[36] I. Syndikus,[7] J. T. Taylor,[17] O. Tengblad,[14] R. Thies,[1] Y. Togano,[31]
M. Vandebrouck,[37] P. Velho,[25] V. Volkov,[7] A. Wagner,[12] F. Wamers,[7,9] H. Weick,[9] C. Wheldon,[24]
G. Wilson,[16] J. S. Winfield,[9] P. Woods,[38] D. Yakorev,[12] M. Zhukov,[1] A. Zilges,[39] K. Zuber,[34]

(R^{3}B Collaboration)

[1] *Institutionen för Fysik, Chalmers Tekniska Högskola, S-412 96 Göteborg, Sweden*
[2] *Departamento de Física de Partículas, Universidade de Santiago de Compostela, 15706 Santiago de Compostela, Spain*
[3] *IGFAE, Instituto Galego de Física de Altas Enerxías,*
Universidade de Santiago de Compostela, 15706 Santiago de Compostela, Spain
[4] *Departamento de Física, Instituto Superior Técnico, Av Rovisco Pais 1, 1049-001 Lisboa, Portugal*
[5] *Centro de Ciências e Tecnologias Nucleares, Universidade de Lisboa,*
Estrada Nacional 10, 2695-066 Bobadela Portugal
[6] *Centro de Física Nuclear, Universidade de Lisboa, PT-1649-003 Lisboa, Portugal*
[7] *Institut für Kernphysik, Technische Universität Darmstadt, 64289 Darmstadt, Germany*
[8] *Institute of Theoretical Physics and Astronomy, Vilnius University, LT-10222 Vilnius, Lithuania*
[9] *GSI Helmholtzzentrum für Schwerionenforschung, D-64291 Darmstadt, Germany*
[10] *Department of Physics, Lund University, S-22100 Lund, Sweden*
[11] *National Superconducting Cyclotron Laboratory,*
Michigan State University, East Lansing, Michigan 48824, USA
[12] *Helmholtz-Zentrum Dresden-Rossendorf, D-01328 Dresden, Germany*
[13] *Department of Physics and Astronomy, Texas A&M University-Commerce, Commerce, Texas 75429, USA*
[14] *Instituto de Estructura de la Materia, CSIC, Serrano 113 bis, E-28006 Madrid, Spain*
[15] *University of Vigo, E-36310 Vigo, Spain*
[16] *Department of Physics, University of Surrey, Guildford GU2 5FH, United Kingdom*
[17] *Oliver Lodge Laboratory, University of Liverpool, L69 3BX, Liverpool, United Kingdom*
[18] *NRC Kurchatov Institute, pl. Akademika Kurchatova, Moscow, Russia*
[19] *Saha Institute of Nuclear Physics, 1/AF Bidhan Nagar, Kolkata-700064, India*
[20] *Justus-Liebig-Universität Gießen, Gießen, Germany*
[21] *Goethe-Universität Frankfurt am Main, 60438 Frankfurt am Main, Germany*
[22] *Astronomy and Physics Department, Saint Marys University, Halifax, Nova Scotia, Canada B3H 3C3*
[23] *Grupo de Física Nuclear & IPARCOS, Universidad Complutense de Madrid, 28040 Madrid, Spain*
[24] *School of Physics and Astronomy, University of Birmingham, Birmingham B15 2TT, United Kingdom*
[25] *Laboratório de Instrumentação e Física Experimental de Partículas - LIP, 1649-003 Lisbon, Portugal.*
[26] *Faculdade de Ciências, Universidade de Lisboa, 1749-016 Lisbon, Portugal*
[27] *Physik Department E12, Technische Universität München, 85748 Garching, Germany*
[28] *KVI-CART, University of Groningen, Zernikelaan 25, NL-9747 AA Groningen, The Netherlands*
[29] *STFC Daresbury Laboratory, Daresbury, Warrington WA4 4AD, United Kingdom*
[30] *Laboratório de Instrumentação, Engenharia Biomédica e Física da Radiação (LIBPhys-UNL),*
Departamento de Física, Faculdade de Ciências e Tecnologias,
Universidade Nova de Lisboa, 2829-516 Monte da Caparica, Portugal
[31] *ExtreMe Matter Institute EMMI, GSI Helmholtzzentrum für Schwerionenforschung GmbH, 64291 Darmstadt, Germany*
[32] *Departamento de FAMN, Universidad de Sevilla, 1065, E-41080, Sevilla, Spain*
[33] *Department of Physics, University of York, Heslington, YO10 5DD, United Kingdom*
[34] *Institut für Kern- und Teilchenphysik, Technische Universität, 01069 Dresden, Germany*
[35] *Frankfurt Institut for Advanced Studies FIAS, Frankfurt, Germany*
[36] *GANIL, CEA/DSM-CNRS/IN2P3, B. P. 55027, 14076 Caen Cedex 5, France*
[37] *GANIL, Bd Henri Becquerel, 14076, Caen, France*

[38]*School of Physics and Astronomy, University of Edinburgh, Edinburgh EH9 3JZ, United Kingdom*
[39]*Institut für Kernphysik, Universität zu Köln, D-50937 Köln, Germany*

Background: For many years, quasi-free scattering reactions in direct kinematics have been extensively used to study the structure of stable nuclei, demonstrating the potential of this approach. The R^{3}B collaboration has performed a pilot experiment to study quasi-free scattering reactions in inverse kinematics for a stable ^{12}C beam. The results from that experiment constitute the first quasi-free scattering results in inverse and complete kinematics. This technique has lately been extended to exotic beams to investigate the evolution of shell structure, which has attracted much interest due to changes in shell structure if the number of protons or neutrons is varied.

Purpose: In this work we investigate for the first time the quasi-free scattering reactions (p,pn) and ($p,2p$) simultaneously for the same projectile in inverse and complete kinematics for radioactive beams with the aim to study the evolution of single-particle properties from $N = 14$ to $N = 15$.

Method: The structure of the projectiles ^{23}O, ^{22}O and ^{21}N has been studied simultaneously via (p,pn) and ($p,2p$) quasi-free knockout reactions in complete inverse kinematics, allowing the investigation of proton and neutron structure at the same time. The experimental data were collected at the R^{3}B-LAND setup at GSI at beam energies of around 400 MeV/u. Two key observables have been studied to shed light on the structure of those nuclei: the inclusive cross sections and the corresponding momentum distributions.

Conclusions: The knockout reactions (p,pn) and ($p,2p$) with radioactive beams in inverse kinematics have provided important and complementary information for the study of shell evolution and structure. For the (p,pn) channels, indications of a change in the structure of these nuclei moving from $N = 14$ to $N = 15$ have been observed; i.e. from the $0d_{5/2}$ shell to the $1s_{1/2}$. This supports previous observations of a sub-shell closure at $N = 14$ for neutron-rich oxygen isotopes and its weakening for the nitrogen isotopes.

I. INTRODUCTION

Quasi-free scattering (QFS) in direct kinematics with stable beams has been demonstrated to be a powerful tool to study the single-particle properties of nuclei along the stability line. In direct kinematics, a proton beam removes a nucleon or a light particle from the target. At around 400 MeV incident energy the probability for nucleon-nucleon collisions within the projectile nucleus should be small [1] and it is generally assumed that the dominant mechanism is due to the quasi-free collision between the proton and the knocked-out particle. This reaction mechanism alone offers the possibility to study not only the outer part but also allows the direct exploration of deeper regions inside the nucleus [1–3]. QFS experiments were first performed in 1952 at Berkeley [2, 4] and showed that if light targets are bombarded with a proton beam with an energy of 340 MeV, proton pairs emerge from the collision with a polar angle of approximately 90°. The opening angle of both particles is not exactly 90° (free scattering) because the collision takes place in the presence of nuclear matter where the proton in the target is not at rest [1]. In 1957, an experiment performed by Tyren, Maris, and Hillman [5] not only proved the validity of the quasi-free interpretation but also demonstrated that it is a fascinating tool to study nuclear shell structure.

Recently, the R^{3}B collaboration [6] undertook a pioneering experiment performing the first ($p,2p$) exclusive measurements with a stable beam of ^{12}C in inverse and complete kinematics [7]. The experiment was performed at the GSI Helmholtzzentrum für Schwerionenforschung facility, in Darmstadt, Germany [8], using the R^{3}B-LAND setup [6]. It is not possible to produce targets of short-lived isotopes, which limits direct reaction studies. This problem can be overcome by using radioactive beams in inverse kinematics. Here, most reaction products are focused in forward direction, which means that a detection system at forward angles, covers almost 4π in the center-of-mass frame. Moreover, fragments produced in the reaction escape from the rather thick target due to their high momentum, which allows the reconstruction of the 4-vectors for all the outgoing particles by measuring their energies and angles. This can be used for a kinematically complete reconstruction of the reaction.

Experimentally, the (p,pn) reaction channel is more challenging than ($p,2p$), due to the difficulty to detect neutrons with good efficiency. Thus, up to now, QFS studies have been mainly restricted to ($p,2p$) reactions. Using a similar setup as for ^{12}C, the R^{3}B collaboration has now performed an experiment where unstable light projectiles at relativistic energies have been investigated in this work via (p,pn) and ($p,2p$) QFS reactions in complete and inverse kinematics.

The evolution of shell structure and its origin has been the subject of many studies. In the light neutron-rich region of the nuclear chart, some exotic nuclei that were expected to be magic are not (as it is the case for ^{12}Be [9, 10]); others, which were not expected to be magic, are (for instance ^{22}O [11]). Recent studies have shown that the proton-neutron interaction plays a major role in magicity, in particular the tensor component [12]. In addition, it has also been shown that the neutron-neutron interaction is important [13]. In particular, experimental and theoretical studies have pursued the study of the shell evolution around $N = 14$, for the oxygen isotopes
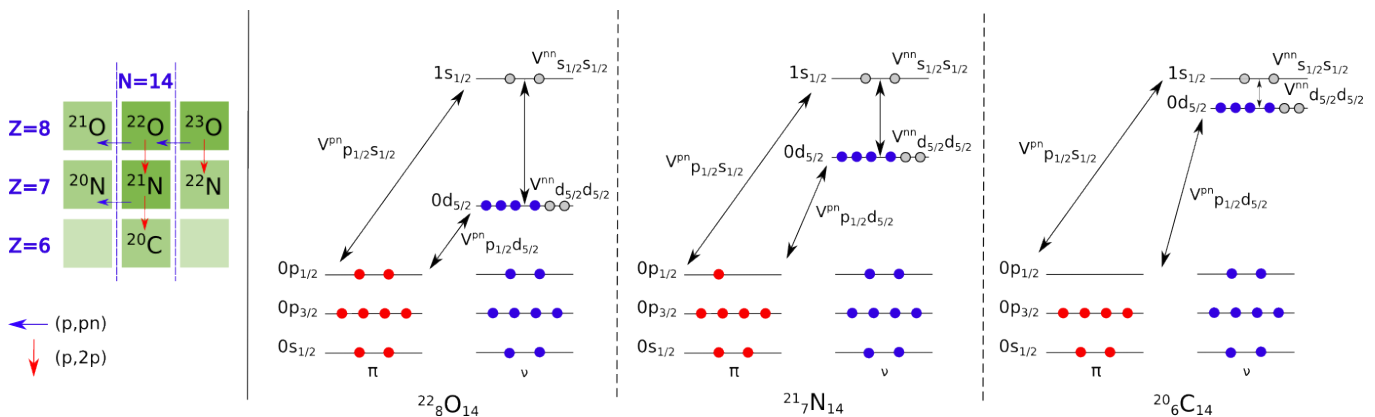
FIG. 1. (Left) Zoom on the nuclear chart area studied in this paper. The projectiles studied simultaneously via (p,pn) (horizontal arrows) and $(p,2p)$ (vertical arrows) are marked in dark shades (dark green shades in the color online version). The fragments produced in the reactions are indicated in a lighter shade (lighter shade of green in the color online version). (Right) Schematic evolution of the $N = 14$ shell gap when protons are removed from the $0p_{1/2}$ while the number of neutrons remains the same. The shaded grey circles represent the nucleons in their corresponding single-particle states that are involved in the (p,pn) reaction.

and isotones. It has been demonstrated that the effective single-particle energies (ESPE) are modified due to the removal of a proton or a neutron from an orbital. Therefore, it is crucial to analyse p-knockout and n-knockout under the same conditions.

It has been observed that the energy of the first 2^+ excited state of ^{22}O (see figure 1 in reference [13]), is almost twice as high as that for ^{20}O and ^{18}O, indicating the appearance of a new shell closure. Based on previous observations on the magicity of $N = 14$ for oxygen isotopes [11], it is interesting to investigate what happens if protons from the $0p_{1/2}$ orbital are removed, producing nitrogen and carbon isotopes (see Fig. 1). For ^{21}N, the 2^+ effective energy (see details in reference [13]) is larger than the one for ^{19}N and ^{17}N; but this increase is not as pronounced as that for the oxygen isotopes, indicating a weakening of the $N = 14$ sub-shell for the nitrogen isotopes [14, 15]. For carbon, it was observed that the energy of the 2^+ state is almost constant for $A = 16$, 18 and 20, indicating the disappearance of the $N = 14$ sub-shell closure. Summarizing, the removal of protons from the $0p_{1/2}$ orbital weakens the $N = 14$ shell closure until it disappears for carbon [16].

Calculations with standard effective interactions (details in Ref. [13]) to obtain the $E(2^+)$ energies show, irrespective of the interaction used, that the gap between the $\nu 1s_{1/2}$ and the $\nu 0d_{5/2}$ orbitals decreases as the number of protons decreases. It is also observed that in this area the $E(2^+)$ experimental data are systematically overestimated by calculations for carbon and nitrogen isotopes (see figure 1 in Ref. [13]). A better agreement with the data requires a reduction of the neutron-neutron monopole interaction term (V_{nn}) in the sd shell. Moreover, that reduction was found to be different for C and N isotopes (0.75 and 0.875, respectively) [13]. The probabilities of the different configurations for the ground states

of ^{20}C, ^{21}N and ^{22}O, calculated using the WBP [17] interaction, show that if the number of protons decreases, the probability of having six neutrons in the $0d_{5/2}$ orbital decreases as well [18]. The mixing of configurations involving the $\nu 0d_{5/2}$ and the $\nu 1s_{1/2}$ orbitals becomes very important for the carbon isotopes. The explanation given is that removing protons from the $\pi 0p_{1/2}$ causes a reduction in the attractive proton-neutron interaction term between the $\pi 0p_{1/2}$ and the $\nu 0d_{5/2}$ [13]. Consequently, the $\nu 0d_{5/2}$ and the $\nu 1s_{1/2}$ orbitals are closer in energy, promoting mixed configurations and decreasing the V_{nn} term (see the right part of figure 1).

The study presented in this work has three main purposes. (i) To assess the feasibility of studying quasi-free proton-nucleon scattering of radioactive beams in inverse kinematics. This will be achieved by analysing both (p,pn) and $(p,2p)$ reactions simultaneously under identical experimental conditions, providing for the first time a comparison of the neutron and proton shells for the same projectile. (ii) The cross sections for both types of processes will be compared to shed light on the differences between the proton and neutron shells. (iii) Shell evolution and magic numbers will be investigated in the region of interest (around $N = 14$).

The theoretical analysis of (p,pN) reactions has been traditionally performed within the distorted-wave impulse approximation (DWIA) [3, 19]. Nowadays, there are different models to study this type of reactions using DWIA [20], DWIA formalism within the eikonal model [21], transfer-to-the-continuum (TC) [22] and Faddeev–Alt-Grassberger-Sandhas (Faddeev/AGS) [23] approaches. In this work, we adopt the Faddeev/AGS formalism [24], which has been used recently in several exploratory studies of (p,pn) reactions [23, 25] and reproduces the experimental transverse momentum distributions for p-knockout from ^{12}C at 400 MeV/u [26]. For

an assumed three-body Hamiltonian (A+p+N), this reaction framework provides a formally exact solution of the scattering problem. The Faddeev/AGS formalism is able to provide the needed angular and energy distributions required to correct our data for the detector response to protons and neutrons.

Up to now the structure of these nuclei has been studied mostly by high-energy heavy-ion induced knockout reactions [27, 28], intermediate-energy one-neutron removal [29, 30] and in-beam γ-ray spectroscopy [11, 14]. In this work, our selected energy domain is expected to promote the QFS mechanism as dominant, probing single-particle orbits in a clean way, not limited to the valence nucleons. This is the first time these nuclei have been studied by this approach. It will be shown that the technique works, in a very interesting region of the chart of the nuclides, giving a glimpse of the possibilities that the new facility FAIR [31] will offer.

II. DESCRIPTION OF THE EXPERIMENTAL SETUP

The primary beam, $^{40}Ar^{+11}$, was provided by the linear accelerator UNILAC (UNIversal Linear ACcelerator). This $^{40}Ar^{+11}$ beam was then injected into the SIS-18 (SchwerIonenSynchrotron) where it was accelerated to an energy of 490 MeV/u with an intensity fluctuating around 10^{10} ions/s and directed to the FRagment Separator (FRS), a high resolution forward-angle spectrometer [32]. At its entrance, a production target of Be, 4.011 g/cm^2 thick, was mounted. When the primary beam impinges on this target, a range of mostly unstable ions are produced by projectile fragmentation. The FRS separated the species of interest depending on their mass-to-charge ratio (A/Q), and those were transported to the experimental area where the R^{3}B-LAND setup is located (see Fig. 2).

Data for six different magnetic rigidity settings centered at different A/Q ratios were collected in the R^{3}B-LAND experimental area.

The velocity of the beam is measured by two position-sensitive plastic scintillators at the exit of the FRS and the entrance of the experimental setup (POS), respectively. An active collimator, ROLU, was used to ensure proper beam alignment. Behind this detector, for tracking and energy loss measurements (ΔE), a position-sensitive silicon detector, PSP, is placed, which allows event-by-event identification of the incoming ions. Then, the beam enters a vacuum chamber where the targets (922 mg/cm^2 CH$_2$ and 935 mg/cm^2 C) were mounted on a remote-controlled target wheel, surrounded by eight double-sided silicon-strip detectors (DSSSDs). The incoming ions of ^{23}O, ^{22}O and ^{21}N reached the target mid-depth with mean energies of 445, 414 and 417 MeV/u and average intensities of approximately 1, 30 and 5 ions/s, respectively. To extract the reactions of the protons in the CH$_2$ target with the projectiles, the contri-

butions from C and from an empty frame must be subtracted. The latter takes into account reactions in the target frame and in the in-beam detectors. The chamber is surrounded by Crystal Ball, a 4π calorimeter which consists of 159 NaI(Tl) crystals, to measure deposited energy (E) and angular distributions (ϕ, θ) of γ rays and light particles (mainly neutrons and protons originating from the QFS reactions). After the reaction, the products traveling in a forward direction are deflected by the ALADIN dipole magnet and, according to their mass and charge, are deflected to one of three arms of the spectrometer. Neutrons are detected by LAND, a Large Area Neutron Detector, heavy fragments are tracked via two scintillating fiber detectors, GFIs, and a time-of-flight wall TFW, while protons are bent further and detected via two proton drift chambers, PDCs, and a second time-of-flight wall, DTF. Therefore all final fragments and their 4-momenta can be extracted.

III. ANALYSIS

The incoming cocktail beam was identified by energy loss in the PSP detector and by ToF measurements between the final focal plane of the FRS and the POS detector. The selection of the desired incoming isotopes was performed by a two-dimensional elliptical cut using the "fragment trigger", which requires a valid signal at POS and TFW. In Fig. 3 an identification plot with Z vs. A/Z is presented for a setting centered on ^{24}O [1].

The outgoing fragments after the reaction target were identified according to their nuclear charge, determined from their energy losses measured in the first DSSSD detector after the target and in the TFW (see Figure 4). For the outgoing fragments, the "Crystal-Ball reaction trigger" was used, which requires "fragment trigger" and an energy signal from the Crystal-Ball detector.

The mass of the outgoing fragments was determined by reconstructing the trajectories of the particles through the ALADIN magnetic field and their paths until they reached the TFW detector, using the R^{3}B-LAND tracker program[2] [33]. To do so, data from the two DSSSDs downstream from the target, as well as from the GFIs and the TFW were used. The tracker needs information about the laboratory positions of the detectors, the nuclear charge of the fragment, the magnetic field maps and the current applied to the magnet to be able to track the events. An example of the outgoing mass distributions in coincidence with the "Crystal-Ball reaction trigger", obtained for the different targets used is shown in Fig. 5.

----

[1] Reproducibility: for unpacking the data, the LAND02 software package with the following git hashes was used: 8ff96c7 and 6d70331. The git hash for the experiment folder was 7e4d07a.

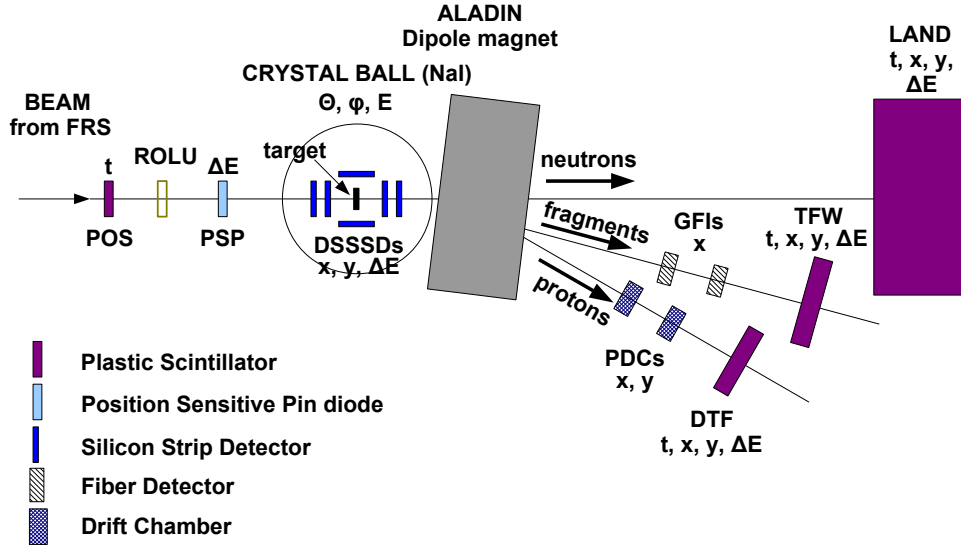[2] Reproducibility: the R^{3}B-LAND tracker software was used with the following git hash a7b74af.

FIG. 2. Schematic drawing of the experimental setup for the experiment (not to scale). Radioactive beams enter the cave from the left. The physical quantities measured by the different detectors are indicated in the figure (for more details see text).
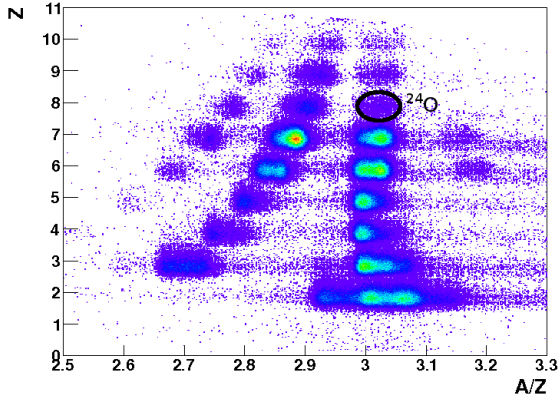

FIG. 3. Incoming identification plot, charge vs. mass-over-charge fraction, for the most exotic setting centered at ^{24}O.
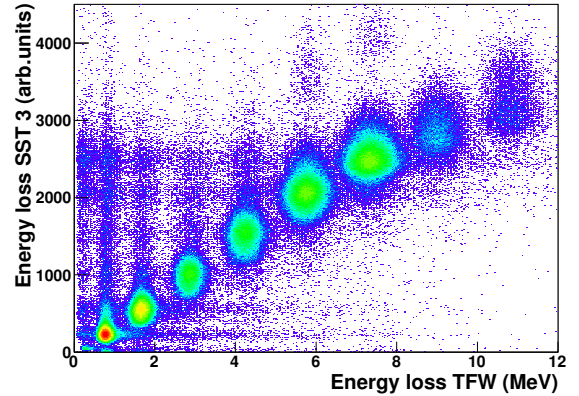

FIG. 4. Energy loss in the first DSSSD behind the target vs. energy loss at the last detector in the setup, the TFW, for the incoming isotope ^{21}N.

A complete identification of the incoming and outgoing nuclei is available at this point of the analysis. The energies and angular distributions of the two outgoing nucleons that do not enter ALADIN are measured by the Crystal Ball detector. To reconstruct the energy and angular distributions of the outgoing nucleons, an addback routine using the nearest neighbouring crystals is used. The algorithm searches for the crystal with the highest energy deposition in an event and adds the energy of the nearest neighbour crystals, which constitute

a cluster. For the reactions of interest, the condition of two high energy depositions, above 20 MeV, is required. Figure 6 shows the polar angle distribution (left) and the azimuthal angle distribution (right) for the representative case of ^{22}O$(p,pn)^{21}$O (top) and ^{22}O$(p,2p)^{21}$N (bottom). In this figure, data from the plastic target with proper subtraction of the contribution from carbon and empty frame measurements are plotted. The negative cross sections originate from statistical fluctuations
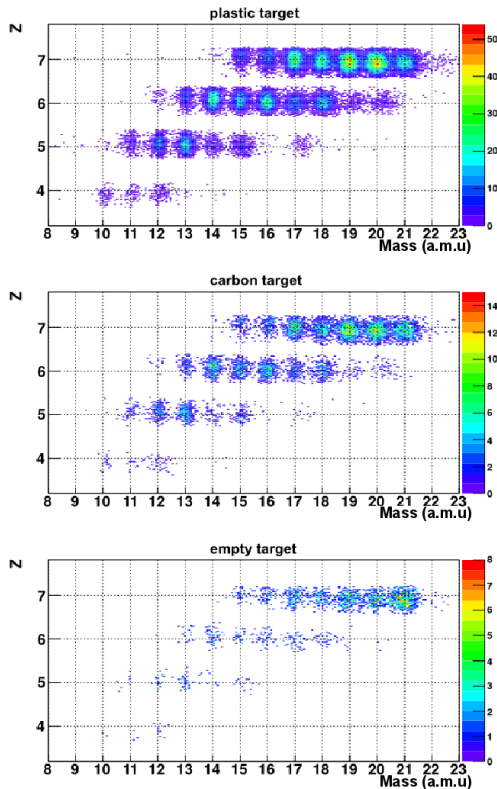
FIG. 5. Charge vs. outgoing mass of fragments after tracking with the "Crystal-Ball reaction trigger" for the plastic, carbon and empty targets, respectively (from top to bottom) when an incoming ^{21}N is used.

in the histogram subtraction needed to obtain the hydrogen distributions. The opening angle peaks around 82°. The azimuthal distribution peaks at 180°. These results demonstrate that the QFS mechanism is dominant in this energy regime. Note that the opening angle for (p,pn) has a contribution at lower angles which is not present (at least with the same strength) for $(p,2p)$. Simulations performed show that for (p,pn), in 21% of the cases the neutron does not deposit the maximum energy in the first NaI crystal that is hit but in a subsequent one, resulting in a limited angular assignment. In most of these cases (61%), the first hit is in a direct neighbour of the crystal with the maximum energy deposition, which still allows for a reasonable angular distribution measurement. The situation is better for protons, where the maximum energy is deposited in the first hit in 93% of the cases. As no angular selection is considered, the results are not affected by the imperfect angular reconstruction of the neutrons.

The cross sections are calculated from the number of reactions and the number of incoming nuclei. The number of incoming nuclei is approximated by the number of unreacted ions after the reaction target, which are

counted at the end of the fragment arm in the TFW detector using the "fragment trigger". As a consequence, the efficiencies of the different detectors, the acceptance, and other effects cancel out because the same detectors and similar conditions are used to perform both countings. This is expected to be a good approximation because the target is sufficiently thin and the energy is high, such that the probability to react in the target is relatively low (in the order of 10^{-2} to 10^{-3}).

The number of reactions was counted using the "Crystal-Ball reaction trigger", which had to be corrected for the response of the Crystal-Ball detector for events with two particles depositing at least 20 MeV in the Crystal-Ball detector array, where response is defined as efficiency × acceptance. To perform the response calculations, two different event generators were used:

- A realistic Monte Carlo event generator, that creates a distribution of particles derived from calculated kinematically fully-exclusive cross sections within the Faddeev/AGS reaction framework (F/A). This formalism has been applied to (p,pn) reactions with stable and exotic projectiles [26, 34, 35].

- A pure kinematic event generator (Kin) that assumes isotropic center-of-mass collisions and employs the Goldhaber model to calculate the width of the momentum distributions [36].

The simulations were performed using the R3BRoot framework[3] [37], which is being developed for simulations and data analysis for the new R^{3}B setup currently under construction at FAIR/GSI [31]. To evaluate the response and its uncertainty, different GEANT4 (geant4-10-01-patch-02) physics lists [38] (BERT 3.0, INCLXX 1.0, BIC 2.0) suitable for the energy range of this work, neutrons and protons up to 700 MeV, were tested. To

TABLE I. Detector responses calculated with the Faddeev/AGS (F/A) and the kinematical (Kin) event generators using the GEANT4 library INCLXX with the high-precision neutron library option and the condition of two particles depositing at least 20 MeV in the Crystal-Ball detector.

Reaction	response F/A (%) INCLXX_HP	response Kin (%) INCLXX_HP
^{22}O$(p,pn)^{21}$O	18	14
^{22}O$(p,2p)^{21}$N	67	58
^{23}O$(p,pn)^{22}$O	–	15
^{23}O$(p,2p)^{22}$N	–	59
^{21}N$(p,pn)^{20}$N	17	14
^{21}N$(p,2p)^{20}$C	66	60

———

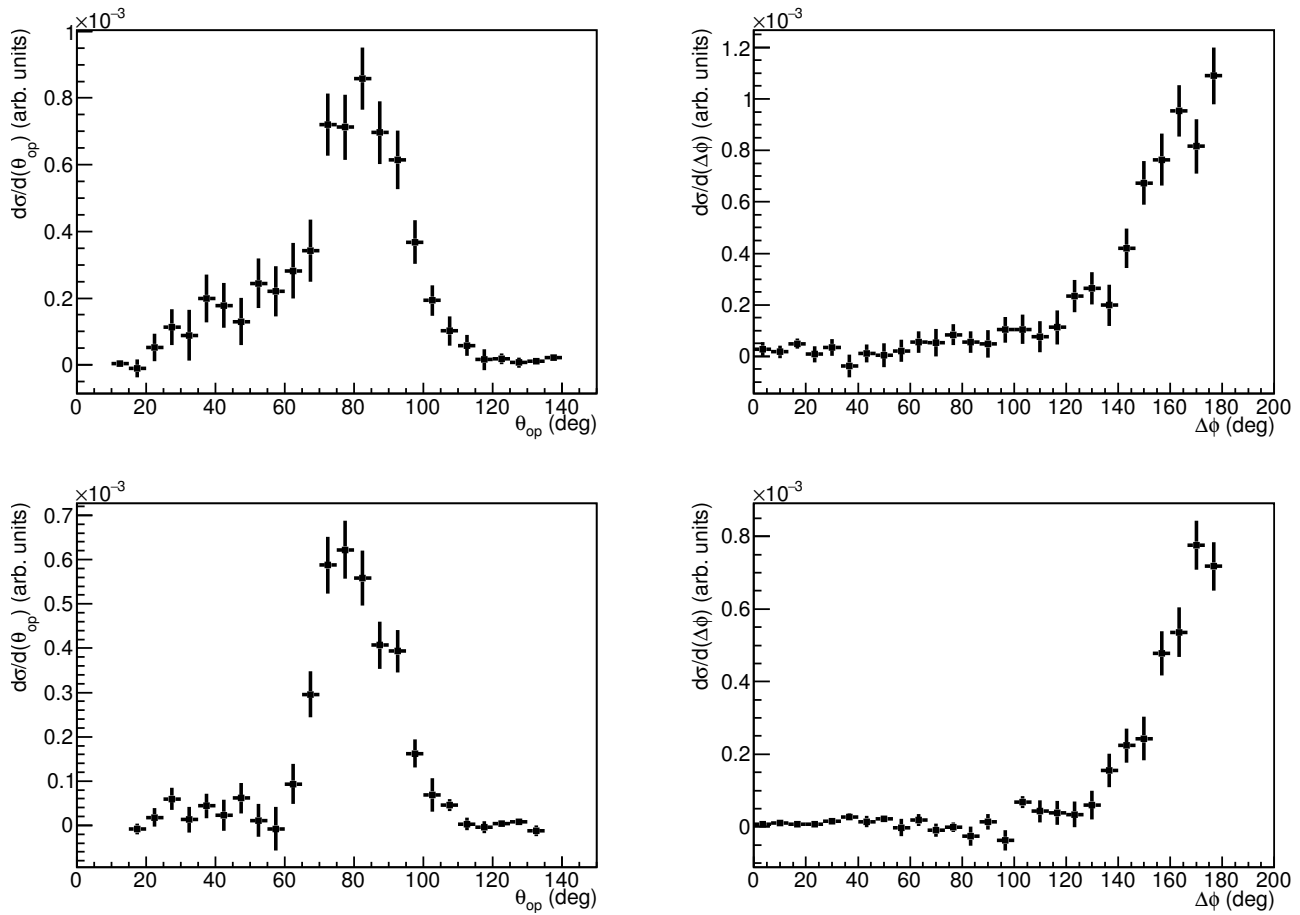[3] Reproducibility: for the simulations the R3BRoot software with the following git hash was used c8034f16ff.

FIG. 6. Polar angle (left) and difference between the azimuthal angles (right) for one neutron and one proton ^{22}O$(p,pn)^{21}$O (top) and two protons ^{22}O$(p,2p)^{21}$N (bottom) in coincidence with the outgoing fragments.

validate the simulation, two different studies were performed. In the first one, the same observables, namely experimental data for energy and multiplicity detected by the Crystal Ball detector, were compared with simulated data. The results indicate that the INCLXX library performs slightly better than the BERT physics list. In order to choose the most suitable physics library, in the second study the experimental efficiency curve obtained in Ref. [39] for neutrons up to 700 MeV impinging on a NaI(Tl) crystal was compared with simulations using different libraries. Given that INCLXX reproduces the experimental efficiency better, all results in this work are based on simulations using INCLXX with the HP option, which uses the high precision library for neutrons. At present, all theoretical input files necessary for the F/A event generator are not available, making it impossible to obtain the response for all studied channels using the F/A event generator. For the cases where both event generators are available, two cross sections will be shown. Table I lists the response values obtained with both generators.

The transverse momentum distributions of the outgo-

ing fragments were obtained from the time-of-flight between the target and the TFW to calculate the velocity and the angular distributions of the fragments measured by the two DSSSDs behind the target, using the tracker program.

The impact point on the target is determined by the two upstream DSSSDs, and the angular distribution of the fragments by the two DSSSDs after the target. In addition to a proper calibration for these detectors, a good relative spatial alignment between them is also needed. This was achieved by performing a linear least squares fit to fragment trajectories in a run without target (unreacted ions), while optimizing the detector positions. Thereby the detectors were shifted virtually based on experimental data.

As the statistics available is very low for most of the reaction channels under study, the root-mean-square (RMS) is used instead of sigma values calculated from Gaussian fits which are commonly used in literature [27, 28] to derive the width of the fragment momentum distributions. In order to extract the RMS, a systematic study of differently-binned histograms was performed.

The RMS has been observed to fluctuate for low bin number but stabilizes afterwards. The average of the RMS values in the stable region is assigned to the width of the momentum distribution. The associated error takes the mean value of the errors and the largest deviation in the errors (for the stable area) into account, which are added quadratically.

IV. RESULTS AND DISCUSSION

The measured inclusive cross sections and widths of the momentum distributions for the one-neutron and one-proton knockout of the projectiles ^{23}O, ^{22}O and ^{21}N are presented in the following (sub)-sections, as well as the fragment momentum distributions. The experimental data will be compared with observables calculated using the Faddeev/AGS reaction framework.

A. One-nucleon knockout inclusive cross sections

The inclusive cross sections of the different n-knockout and p-knockout channels are determined from the number of reactions in a given target induced by a measured number of incoming ions. The resultant inclusive cross sections, uncorrected σ_{raw} as well as $\sigma_{\mathrm{F/A}}$ and σ_{Kin} corrected for the Crystal Ball detector response using the two different event generators F/A or Kin, respectively, are shown in Table II. The uncertainties in the table are statistic (first number) and systematic (second number). For the oxygen projectiles the results were obtained using two independent analyses performed within the collaboration with different cuts and statistical methods checking for consistency. Both methods return similar values. The values of the cross sections and the uncertainties in both methods have been combined to obtain the results presented in this paper. The systematic uncertainty given in Table II accounts for the small difference between the two procedures. The left part of Fig. 7 presents the total inclusive cross sections for the one-neutron (top) and one-proton (bottom) knockout as a function of the neutron and proton number of the projectile, respectively.

1. (p,pn) vs (p,2p)

Independently of the NaI response function considered, the cross sections of the one-neutron knockout channel are systematically larger than those for one-proton knockout for a given projectile as expected from the large neutron excess of the nuclei under study. The third column of Table II presents the measured cross sections for the investigated $(p,2p)$ and (p,pn) reactions without any corrections for the response of the Crystal-Ball detector. Given that the probability for detecting a proton in NaI is larger than detecting a neutron at the given energies,

taking any response function into account will just increase this trend in the data, as can be observed in the fourth and fifth columns of Table II.

The difference between the (p,pn) and $(p,2p)$ cross sections can be explained in a simplified mean field picture considering neutrons in the psd-shell. All projectiles are neutron-rich nuclei and, therefore, there are more neutrons than protons available for reactions. Also, the neutron $0d_{5/2}$ orbital is almost full for the cases under study, giving rise to large spectroscopic factors for neutrons removed from this orbital (see shell model calculations in section IV C). Moreover, the binding energy of the outermost neutrons is smaller than that of the protons. As a result, neutron-knockout is favoured.

Another difference between the (p,pn) and $(p,2p)$ cases, that favors (p,pn) over $(p,2p)$, stems from the difference between the p-n and p-p interactions. Between 400 MeV and 500 MeV, the np scattering cross section is around 27% larger than that for pp scattering [40]. On the other hand, all kinematic contributions of the emitted light fragments have to be evaluated accurately. It was shown in Refs. [21, 34] that the absorption part of the nucleon-nucleus potential produces a reduction of the (p,pn) inclusive cross section, compared to the Plane Wave Impulse Approximation (PWIA). This reduction becomes increasingly important as a function of the binding energy of the knocked-out nucleon [35], so this is another factor that needs to be taken into account when comparing the (p,pn) and $(p,2p)$ cross sections.

2. (p,pn)

In the oxygen isotopic chain ($Z = 8$), the (p,pn) cross section is larger for $N = 15$ than for $N = 14$, independent of the adopted response correction. This can be understood in a simplified shell model picture where $N = 14$ is interpreted as a closed sub-shell with a dominating configuration of a completely-filled $0d_{5/2}$ level containing six neutrons, while $N = 15$ has a single additional neutron in the $1s_{1/2}$ orbital. Another argument supporting this approach is the fact that, according to [34], the PWIA cross section is approximately the same for different projectiles but corrections reduce the cross section as a function of the separation energy. The fact that the cross section of $N = 15$ is larger than the one for $N = 14$ for the oxygen isotopes is an indication of the existence of a sub-shell at $N = 14$, $Z = 8$ — an observation already discussed in Ref. [11].

For $N = 14$ and $Z = 7$ or $Z = 8$ the n-knockout cross section increases when the proton number decreases. This can be explained in terms of configuration mixing. Calculations performed by Yuan et al. [18] show that the probability of the valence neutrons to fully occupy the $0d_{5/2}$ level decreases when a proton is removed from the $0p_{1/2}$ orbital passing from oxygen to nitrogen. This could be an indication of the weakening of the $N = 14$ sub-shell for $Z = 7$.

TABLE II. Inclusive cross sections for the one-neutron and one-proton knock-out channels for the projectiles ^{23}O, ^{22}O and ^{21}N at 445, 414 and 417 MeV/u impinging on protons in the target, uncorrected and corrected for the Crystal Ball detector response. σ_{raw}, $\sigma_{\mathrm{F/A}}$ and σ_{Kin} stand for the inclusive cross sections without and with the Crystal-Ball detector response, while F/A and Kin indicate which generator was used for the correction. Uncertainties in the table are statistical (first number) and systematic (second number).

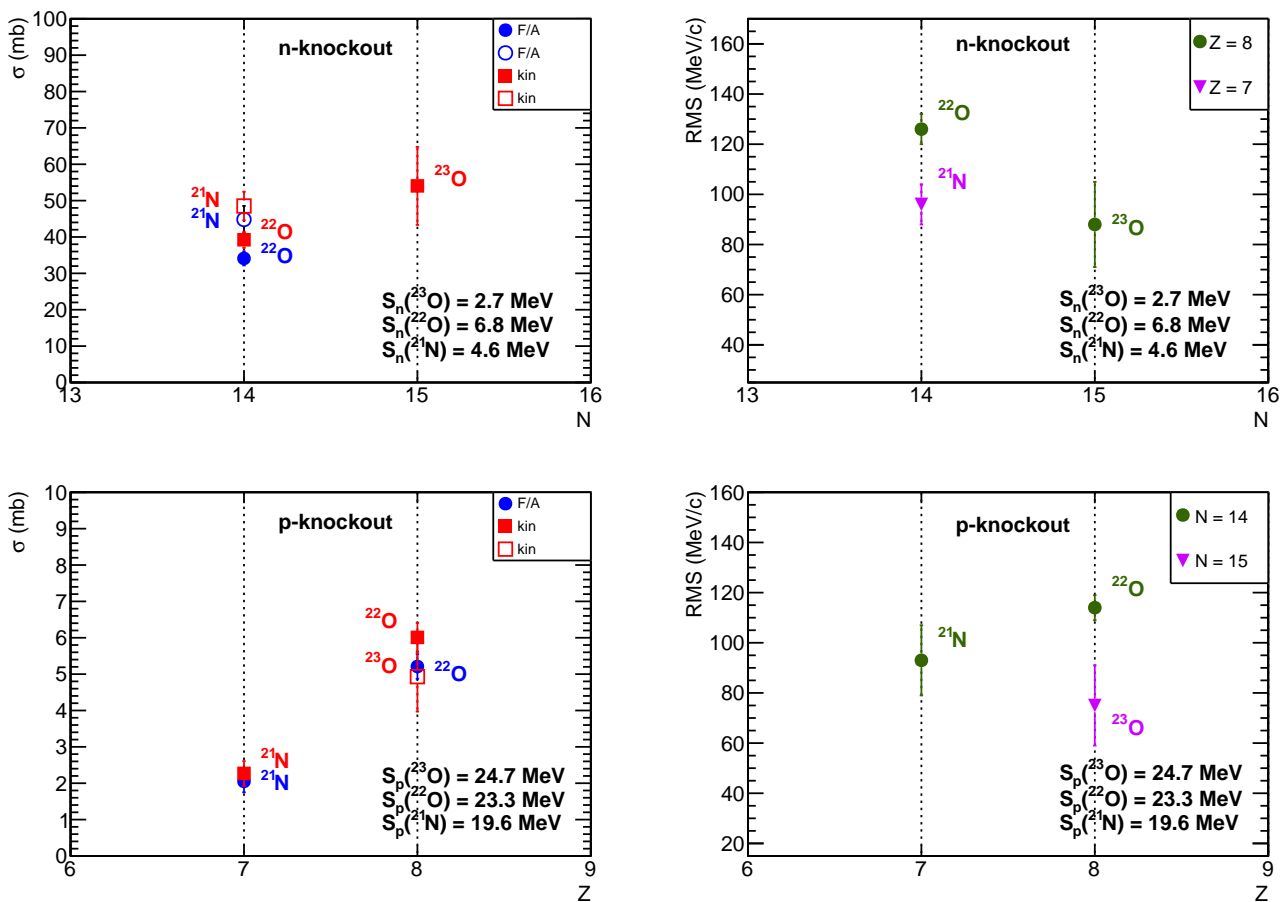| E_{beam} (MeV/u)	Reaction	σ_{raw} (mb)	$\sigma_{\mathrm{F/A}}$ (mb)	σ_{Kin} (mb)
445	^{23}O$(p,pn)^{22}$O	9.0±1.8±0.9	–	54.0±10.7±1.1
	^{23}O$(p,2p)^{22}$N	3.04±0.59±0.05	–	4.93±0.96±0.10
414	^{22}O$(p,pn)^{21}$O	6.22±0.25±0.44	34.1±1.9±0.7	39.2±2.2±0.8
	^{22}O$(p,2p)^{21}$N	3.49±0.23±0.08	5.21±0.34±0.10	6.01±0.40±0.12
417	^{21}N$(p,pn)^{20}$N	7.55±0.61	44.8±3.6±0.9	48.5±3.9±1.0
	^{21}N$(p,2p)^{20}$C	1.35±0.20	2.05±0.30±0.04	2.27±0.34±0.04

FIG. 7. Top: cross sections (left) and RMS (right) for the one-neutron knockout channel as a function of the neutron number for the projectiles ^{21}N and ^{23,22}O. Bottom: cross sections (left) and RMS (right) for the one-proton knockout channel as a function of the proton number for the projectiles ^{21}N, ^{23,22}O. In both cases, the one neutron (proton) separation energy for each projectile is included in the plot, taken from [41]. The generator used for the response of the Crystal-Ball detector used in the cross section calculation is indicated in the legend.

3. (p,2p)

The one-proton knockout results show very similar cross sections for the oxygen isotopes and a smaller one for ^{21}N. The valence protons of all these projectiles reside in the same orbital. In the oxygen isotopes the two least-bound protons completely fill the $0p_{1/2}$ orbital, while ^{21}N

has one proton less in this single-particle level. Under the assumption of a simple mean field picture and that adding one neutron does not modify the proton orbitals, one might expect that the total cross section contributions for p-knockout from the ^{22}O ($N = 14$) and ^{23}O ($N = 15$) isotopes to be identical and what we observe is an agreement within error bars. In addition, when comparing the p-knockout from the two isotones ^{21}N ($Z = 7$) and ^{22}O ($Z = 8$), the fact that $Z = 8$ has a larger cross section than $Z = 7$ indicates that it is more probable to remove a proton from oxygen because of the higher occupancy even if the separation energy is larger.

B. Momentum distributions

The momentum distributions of the fragments provide direct insight into the relative wave function of the struck nucleon, in the limit where the QFS mechanism is dominant. Experimentally, the total momentum distributions of the fragments are obtained by the tracking program. The experimental setup has a better resolution for the transverse component of the momentum than for the longitudinal. Thus, the following discussion will be based on the results extracted for the vertical transverse component. In Fig. 8, the transversal momentum distributions for all reaction channels studied in this paper are shown.

In Table III and Fig. 7 the results obtained for the Root Mean Square (RMS) of the transverse momentum distributions for all different channels are presented. The RMS values given in the third column are corrected for the straggling in the materials surrounding the target area, taken as the RMS of the unreacted beam without target.

TABLE III. Transverse momentum distribution RMS for the one-neutron and one-proton knockout reactions for the projectiles ^{22}O, ^{23}O and ^{21}O. In the third column the RMS of the unreacted beam distribution without target has been subtracted, w.s.; stands for without straggling.

Reaction	RMS (MeV/c)	RMS$^{\text{w.s.}}$ (MeV/c)
^{22}O$(p,pn)^{21}$O	132±5	126±6
^{22}O$(p,2p)^{21}$N	120±5	114±5
^{23}O$(p,pn)^{22}$O	96±16	88±17
^{23}O$(p,2p)^{22}$N	84±14	75±16
^{21}N$(p,pn)^{20}$N	102±8	96±8
^{21}N$(p,2p)^{20}$C	99±13	93±14

1. (p,pn)

For the two oxygen isotopes the momentum RMS decreases with increasing neutron number. This can be explained within the adopted shell model context. The $N = 14$ valence neutrons populate mainly the $0d_{5/2}$ level, while the single valence neutron for $N = 15$ is in the $1s_{1/2}$ orbital. This change from the d shell (angular momentum $\ell = 2$) to the s shell (angular momentum $\ell = 0$) explains the narrowing in the momentum distributions. To obtain more insight into the single particle contributions to the momentum distributions, in Fig. 9 the fit to the experimental data using the theoretical momentum distributions calculated in the Faddeev/AGS reaction framework (see next section) with a spectroscopic factor equal to one [35] is presented. For ^{22}O, a larger contribution of $\ell = 2$ of 85±12% corresponding to the ^{21}O($5/2^+$,g.s.) $\otimes$ $d_{5/2}$ configuration and 15±12% for the ^{21}O($1/2^+$,exc.) $\otimes$ $s_{1/2}$ configuration are observed. The case of the ^{23}O projectile is more difficult to analyze due to the poor statistics. The obtained weights are 79±21% for the d-wave and 21±21% for the s-wave, compatible with an enhancement of the $\ell = 0$ component. Therefore, theoretical calculations support the explanation given above. Comparisons with previous experimental results from breakup and one-neutron removal reactions [27, 28] show a good agreement with our results. The ratio of the momentum width from ^{22}O to ^{23}O is 1.55±0.14 and 1.53±0.39 in Ref. [27] and Ref. [28], respectively. Ref. [29] provides results for the longitudinal and transversal momentum distributions of 1.74±0.12 and 1.48±0.26, respectively. These numbers are all in agreement with our result of 1.43±0.28.

From the comparison of the $N = 14$ nuclei with different Z, it can be observed that the width of the momentum distribution for $Z = 7$ is smaller than that for $Z = 8$. This can be explained in terms of the mixing of different configurations that are present in ^{21}N. This nucleus has a lower contribution from the d-wave compared with the ^{22}O, implied by the RMS reduction. This can also be an indication of the weakening of the $N = 14$ sub-shell if a proton is removed from the full $0p_{1/2}$ in oxygen to produce nitrogen.

2. (p,2p)

Focusing our attention first on the $N = 14$ shell, the RMS for ^{22}O is larger than that for ^{21}N. An explanation could be that the oxygen isotope has its valence sub-shell full, rendering the nucleus tightly bound, i.e. more compact, which translates into a wider momentum distribution. Despite the very low number of events for the one-proton knockout channel from ^{23}O, the data indicate a very narrow momentum distribution of 75±16 MeV/c. This is, within error bars, in agreement with our model calculations, but significantly narrower than that for ^{22}O with 114±5 MeV/c.
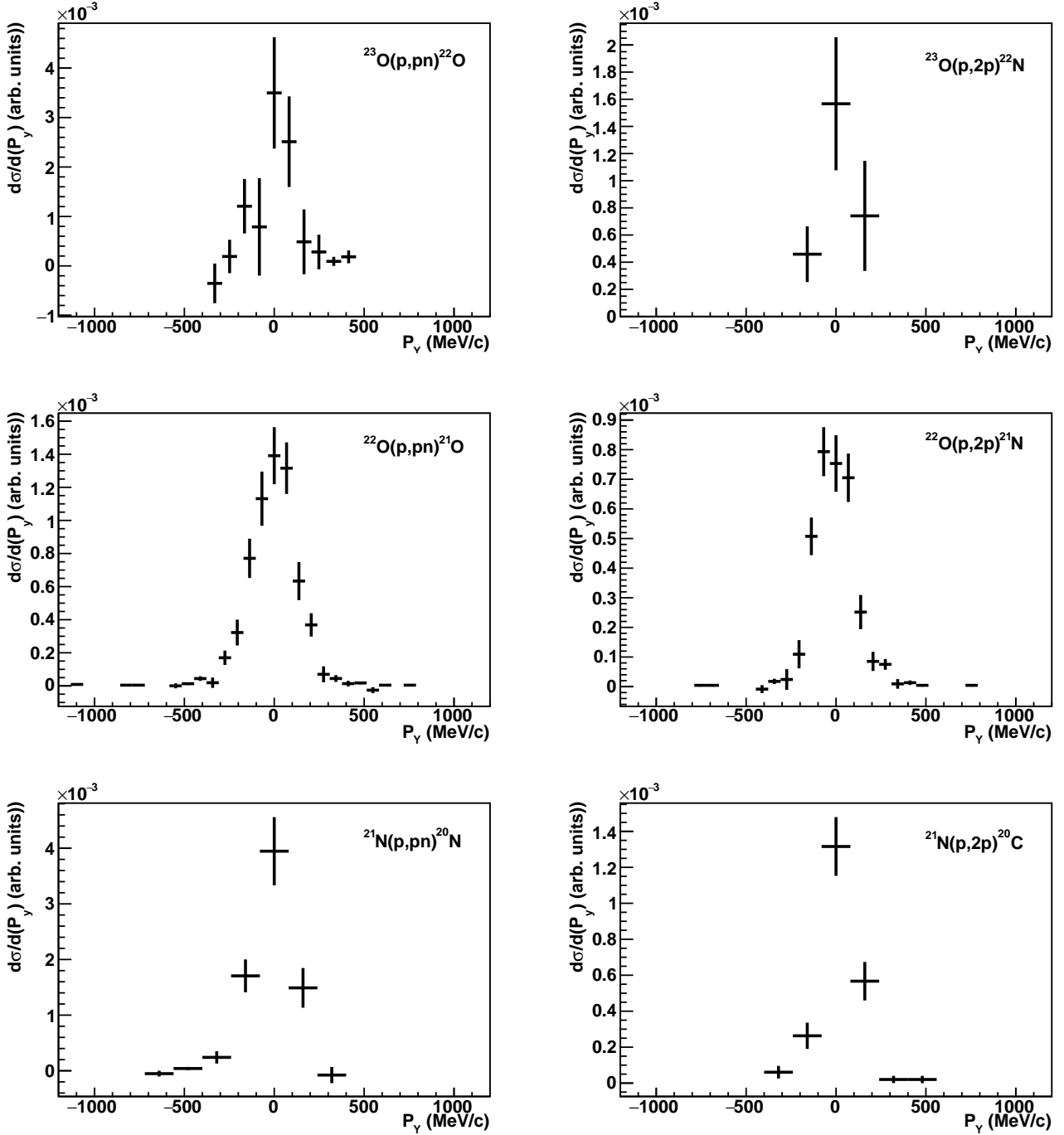
FIG. 8. Transverse momentum distributions for all (p,pN) channels. The (*p,pn*) channels are on the left, while (*p,2p*) channels are on the right.

C. Reaction analysis and shell model calculations

The theoretical observables (cross sections and fragment momentum distributions) for the knockout of a nucleon from a given shell were obtained within the three-body non-relativistic Faddeev/AGS reaction framework [24]. For nucleon knockout from a nucleus A due to the collision with a proton target, the dominance of the QFS reaction mechanism presupposes that only a limited number of particles participate in the scattering process, the heavy fragment (HF) assumed to be inert, the target proton p and the emitted nucleon N. In addition, it is assumed that the scattering is determined by the p-N scattering distorted by the HF. In this case one expects

TABLE IV. Shell-model spectroscopic factors C^2S (which include the isospin C^2 and center of mass corrections [45]). Excitation energies E_c and spin-parity I_c^π obtained as well from shell-model calculations. Single-particle cross sections σ_{sp}, theoretical total inclusive cross sections σ_{th}, experimental total inclusive cross sections σ_{exp} for F/A and Kin generators and ratio between experimental and theoretical cross sections for both generators. For states marked with * the σ_{sp} of the first state with the same I_c has been used. This is considered a good approximation because the difference in separation energy for those states is relatively small. Only states with spectroscopic factors larger than 0.01 and with excitation energies below the neutron or proton separation energy are shown.

^{A}X	$^{A-1}$X	E_c (MeV)	I_c^π	$n\ell j$	C^2S	σ_{sp}(mb)	σ_{th}(mb)	$\sigma_{exp,F/A}$(mb)	$\sigma_{exp,F/A}/\sigma_{th}$	$\sigma_{exp,Kin}$(mb)	$\sigma_{exp,Kin}/\sigma_{th}$
							(p,pn)				
^{23}O	^{22}O	0.0	0_1^+	$1s_{1/2}$	0.87	15.4					
		3.4	2_1^+	$0d_{5/2}$	2.27	12.1					
		4.6	0_2^+	$1s_{1/2}$	0.13	15.4*					
		4.8	3^+	$0d_{5/2}$	3.37	12.1*	98.8	–	–	54.0±10.8	0.55±0.11
		5.8	1^-	$0p_{1/2}$	0.82	10.5					
		6.1	0^-	$0p_{1/2}$	0.33	10.4					
		6.5	2_2^+	$0d_{5/2}$	0.26	12.1*					
^{22}O	^{21}O	0.0	$5/2^+$	$0d_{5/2}$	5.73	11.5	69.0	34.1±2.0	0.49±0.03	39.2±2.3	0.57±0.03
		1.5	$1/2^+$	$1s_{1/2}$	0.25	12.6					
^{21}N	^{20}N	0.0	2^-	$0d_{5/2}$	1.97	12.7					
		0.6	0^-	$1s_{1/2}$	0.16	14.8	72.5	44.8±3.7	0.62±0.05	48.5±4.0	0.67±0.06
		0.9	3^-	$0d_{5/2}$	2.98	12.7*					
		1.1	1^-	$1s_{1/2}$	0.49	14.8*					
							(p,2p)				
^{23}O	^{22}N	0.0	0^-	$0p_{1/2}$	0.50	6.3	12.5	–	–	4.93±0.96	0.39±0.08
		0.8	1^-	$0p_{1/2}$	1.48	6.3*					
^{22}O	^{21}N	0.0	$1/2^-$	$0p_{1/2}$	1.87	6.23	15.8	5.21±0.36	0.32±0.02	6.01±0.41	0.38±0.03
		1.9	$3/2^-$	$0p_{3/2}$	0.73	6.0					
^{21}N	^{20}C	0.0	0^+	$0p_{1/2}$	0.72	6.8	7.0	2.05±0.31	0.29±0.04	2.27±0.34	0.32±0.05
		2.2	2^+	$0p_{3/2}$	0.33	6.5					

a polar and azimuthal angle distributions as the ones obtained experimentally and shown in Figure 6. Results of the same type were also obtained theoretically for nucleon knockout from ^{12}C [26]. Some details of this approach are discussed in the following.

The knockout of a nucleon from a projectile, consisting of a core and a nucleon, can be formulated as a three-body scattering problem. In our approach, the core can be either in the ground or a low-lying excited state. Core excitations during the collision, i.e. dynamic excitations, are not considered. For proton knockout only the Coulomb interaction between the core and the proton target is included. As mentioned above, relativistic effects are not taken into account. Before solving the Faddeev/AGS equations the interactions between the knocked-out nucleon and the target proton (N-p), between the knocked-out nucleon and the core (N-core), and between the core and the target proton (core-p) must

be specified. The realistic nucleon-nucleon CD Bonn potential [42] is used for the N-p reaction pair. Note that the p-p interaction acts in isospin triplets only, while the p-n interaction acts also in isospin single partial waves, which contribute significantly to the cross section. The potential that models the interaction between the valence nucleon and the core is taken as local and ℓ-dependent. In a partial wave where a bound state occurs, the potential is real with a central part. In all other partial waves the potential may have both real and imaginary components. The parametrization to describe the p-core and N-core interactions is not known. In this work we employ the same parametrisation of the optical potentials if the core is either in the ground or in any excited state. The standard Faddeev/AGS framework requires an energy independent interaction for both p-core and N-core interactions. We employ, as in Ref. [26], the Koning-Delaroche parametrization of the optical poten-
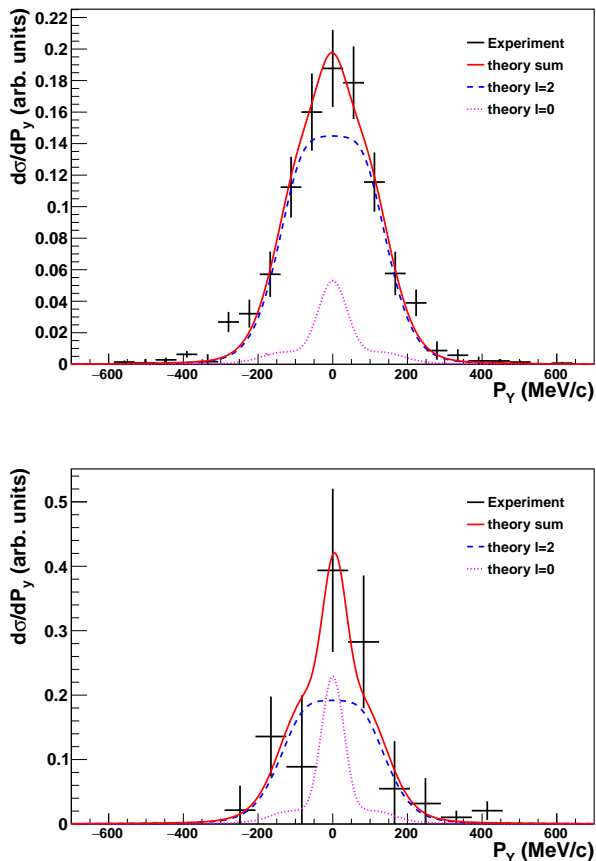
FIG. 9. Transverse momentum distribution for the projectile ^{22}O (top) and for the ^{23}O (bottom) in the (p,pn) reaction with the Crystal Ball detector in coincidence. The solid line (red) represents the fit of the dashed (blue) and dotted (pink) lines corresponding to the calculated $\ell = 2$ and $\ell = 0$ contributions convoluted with the experimental resolution, respectively.

tial at a fixed energy of 200 MeV for p-core and N-core interactions. Note that different parametrizations can reproduce the momentum distributions, although with different weight for each final state configuration of the HF [26].

The spectroscopic factors $C^2S(I_c^\pi, nlj)$ were obtained from shell model calculations using the code Oxbash [43] and the WBT [44] interaction. The model space used for the calculations included the spsdpf orbitals, with restrictions $(0+1)\hbar\omega$ for the ^{23}O(p,pn), ^{23}O$(p,2p)$, ^{22}O(p,pn), ^{22}O$(p,2p)$ and ^{21}N(p,pn) or $(0+2)\hbar\omega$ for ^{21}N$(p,2p)$. The single particle configurations and the $C^2S(I_c^\pi, nlj)$ are shown in Table IV.

We define a theoretical cross section as the product of the calculated full cross section for a given shell multiplied by the corresponding spectroscopic factor and summed over all single particle configurations considered:

$$\sigma_{th}(p,pN) = \sum_{nlj,I} C^2S(I, nlj)\sigma_{sp}(I, nlj). \qquad (1)$$

The theoretical cross sections, combination of the single-particle cross sections from Faddeev/AGS and the shell model spectroscopic factors, shown in table IV are in agreement with the cross sections trends observed in figure 7. The experimental cross sections divided by the theoretical ones were calculated as well. Deviations from unity indicate the inadequacy of either the structure model or the reaction framework and parameters. The results are given in Table IV. A detailed comparison of the Faddeev/AGS theory and the experiment is foreseen in a forthcoming paper. We anticipate discussing the reduction factors obtained using this reaction framework in comparison with those obtained by other model approaches, as well as a comparison with the data discussed in Ref. [46].

V. CONCLUSIONS AND OUTLOOK

Light neutron-rich nuclei around $N = 14$ (^{23}O, ^{22}O and ^{21}N) have been investigated for the first time via quasi-free scattering of both $(p,2p)$ and (p,pn) reactions to study their proton and neutron shell structure, respectively. The modification in the structure of these nuclei from $N = 14$ to $N = 15$ has been studied by measuring the inclusive cross sections and the momentum distribution of the remaining fragments. The occupation of the $0p_{3/2}$, $0p_{1/2}$ proton orbitals has been investigated using $(p,2p)$ reactions.

The results obtained for the cross sections are shown in Table II. The inclusive cross sections obtained for the (p,pn) channels are larger than those obtained for $(p,2p)$ reactions. This fact can be explained based on a simplified mean field picture and is consistent with calculated total cross sections from a combination of the Faddeev/AGS single particle cross sections multiplied by the shell model spectroscopic factors shown in Table IV. It was observed for the neutron shells, in the (p,pn) reactions, that ^{23}O has the largest measured cross section found in this work, which might be explained by a correspondingly lower separation energy, and that the other two nuclei (^{22}O and ^{21}N) have valence neutrons in a closed orbital. The comparison of the cross sections for ^{22}O and ^{21}N shows an increment, which is consistent with a weakening of the $N = 14$ sub-shell when a proton is removed from the $0p_{1/2}$. For the $(p,2p)$ channels we found that the nuclei with $Z = 8$ have approximately the same cross section, since they have similar proton configurations. Those cross sections are larger than that for ^{21}N due to the larger number of valence protons that can contribute to the reaction.

Regarding the momentum distributions, it was observed for the (p,pn) channels that the RMS decreases from $N = 14$ to $N = 15$, consistent with the results for the inclusive cross sections. This can be interpreted as neutrons passing from the d-shell to the s-shell, which has a wider spatial distribution and hence a narrower momentum distribution. The two nuclei with $N = 14$ show

an RMS trend consistent with the weakening of that sub-shell for nitrogen isotopes. The extracted contributions of the different orbitals are consistent with previous measurements [27–29]. The Faddeev/AGS calculations were able to reproduce the shape of the momentum distributions.

We have in this paper demonstrated that the simultaneous study of (p,pn) and $(p,2p)$ reactions is an useful and complementary tool to shed light on nuclear structure. Improvements in the experimental setup, which will be available in the future, will help to perform measurements with significantly improved statistics and better resolution.

[1] G. Jacob and T. A. J. Maris, Rev. of Mod. Phys., 38, 121 (1966).
[2] O. Chamberlain and E. Segrè., Phys. Rev. 87, 81 (1952).
[3] G. Jacob and T. A. J. Maris, Rev. of Mod. Phys., 45, 6 (1973).
[4] J. B. Cladis, W. N. Hess, and B.J.Moyer, Phys. Rev. 87, 425 (1952).
[5] H. Tyrén, T. A. J. Maris and P. Hillman, II Nuovo Cimento, 6, 1507 (1957).
[6] http://www.gsi.de/r3b.
[7] V. Panin, J. T. Taylor, S. Paschalis, F. Wamers, Y. Aksyutina, H. Alvarez-Pol, T. Aumann, C. A. Bertulani, K. Boretzky, C. Caesar, M. Chartier, L. V. Chulkov, D. Cortina-Gil, J. Enders, O. Ershova, H. Geissel, R. Gernhäuser, M. Heil, H. T. Johansson, B. Jonson, A. Kelic-Heil, C. Langer, T. Le Bleis, R. Lemmon, T. Nilsson, M. Petri, R. Plag, R. Reifarth, D. Rossi, H. Scheit, H. Simon, H. Weick, C. Wimmer, Phys. Lett. B 753, 204 (2016).
[8] GSI, Helmholtzzentrum für Schwerionenforschung http://www.gsi.de.
[9] A. Navin et al., Phys. Rev. Lett. 85 (2000) 266.
[10] S. D. Pain et al., Phys. Rev. Lett. 96, 032502 (2006).
[11] M. Stanoiu et al., Phys. Rev. C 69, 034312 (2004).
[12] T. Otsuka, T. Suzuki, R. Fujimoto, H. Grawe, Y. Akaishi, Phys. Rev. Lett. 95, 232502 (2005).
[13] C. X. Yuan, C. Qi, F. R. Xu, Nuc. Phys. A Vol 883, 25 (2012).
[14] D. Sohler et al., Phys. Rev. C 77, 044303 (2008).
[15] C. Rodriguez-Tajes et al., Phys. Rev. C 83, 064313 (2011).
[16] M. Stanoiu et al., Phys. Rev. C 78, 034315 (2008).
[17] E. K. Warburton and B. A. Brown, Phys. Rev. C 46, 923 (1992).
[18] C. X. Yuan, F. R. Xu, C. Qi, Journal of Phys. Conf. Series 420, 012049 (2013).
[19] N.S. Chant and P.G. Roos, Phys. Rev. C 15, 57 (1977).
[20] Kazuyuki Ogata, Kazuki Yoshida, and Kosho Minomo, Phys. Rev. C 92, 034616 (2015).
[21] T. Aumann, C. A. Bertulani and J. Ryckebusch, Phys. Rev. C 88, 064610 (2013).
[22] A. M. Moro, Phys. Rev. C 92, 044605 (2015).
[23] R. Crespo, A. Deltuva, E. Cravo, M. Rodríguez-Gallardo, A.C. Fonseca, Phys. Rev. C 77, 024601 (2008).
[24] L. D. Faddeev. Zh. Eksp. Teor. Fiz. 39, 1459 (1960).
[25] R. Crespo, A. Deltuva, M. Rodríguez-Gallardo, E. Cravo, A.C. Fonseca, Phys. Rev. C 79, 014609 (2009).
[26] R. Crespo, E. Cravo, A. Deltuva, Submitted to Phys. Rev C (2016).
[27] D.Cortina-Gil et al., Phys. Rev. Lett. 93, 062501 (2004).
[28] C. Rodríguez-Tajes et al., Phys. Rev. C 82, 024305 (2010).
[29] E. Sauvan et al., Phys. Rev. C 69, 044603 (2004).
[30] E. Sauvan et al., Phys. Lett. 491B, 1 (2000).
[31] http://www.fair-center.eu/.
[32] H. Geissel et al., Nucl. Instr. Meth. B 70, 286 (1992).
[33] R. Plag, Documentation on the LAND R^{3}B tracker, GSI 2015, http://ralfplag.de/tracker.
[34] E. Cravo, R. Crespo and A. Deltuva, Phys. Rev. C 93, 054612 (2016).
[35] R. Crespo, A. Deltuva and E. Cravo, Phys. Rev. C 90, 044606 (2014).
[36] L.V. Chulkov et al., Nucl. Phys. A 759, 43 (2005).
[37] https://www.r3broot.gsi.de/.
[38] S. Agostinelli et al., Nucl. Inst. and Meth. A 506, 250 (2003).
[39] P. P. Dunphy, E. L. Chupp, M. Popecki, D. J. Forrest, D. Lopiano, T. Shima, H. Spinka, G. Glass, G. Burleson,

M. Beddo, Exp. Astr. 1992, 2, 233258.

[40] S. K. Charagi, S. K. Gupta, Phys. Rev. C 41, 1610 (1990).

[41] National Nuclear Data Center, information extracted from the NuDat 2 database, http://www.nndc.bnl.gov/nudat2/.

[42] R. Machleidt, Phys. Rev. C 63, 024001 (2001).

[43] A. Etchegoyen, W. D. M. Rae, N. S. Godwin, W. A. Richter, C. H. Zimmerman, B. A. Brown, W. E. Ormand, and J. S. Winfield, MSU-NSCL Report 524 (1985).

[44] E.K. Warburton and B.A. Brown, Phys. Rev. C 46, 923 (1992).

[45] A. E. L. Dieperink and T. de Forest, Jr. Phys. Rev. C 10, 543 (1974).

[46] L. Atar et al., Phys. Rev. Lett., (in press).